Water Evolution in Direct Methanol Fuel Cell Cathodes studied by Synchrotron X-ray Radiography

A. Schröder[a], K. Wippermann[a]*, T. Arlt[b], T. Sanders[c], T. Baumhöfer[c], H. Markötter[b], J. Mergel[a], W. Lehnert[a], D. Stolten[a,d], I. Manke[b], J. Banhart[b,e]

[a]Institute of Energy and Climate Research, IEK-3: Fuel Cells, Forschungszentrum Jülich GmbH, 52425 Jülich, Germany

[b]Helmholtz-Zentrum Berlin, Institut für Angewandte Materialforschung, Hahn-Meitner-Platz 1, 14109 Berlin, Germany

[c]Institute for Power Electronics and Electrical Drives (ISEA), RWTH Aachen University, Jägerstraße 17–19, 52066 Aachen, Germany

[d]Chair for Fuel Cells, RWTH Aachen University, Germany

[e] Technische Universität Berlin, Straße des 17.Juni 135, 10623 Berlin, Germany

*corresponding author; tel.: +49 2461 61 2572; fax: +49 2461 61 6695; e-mail address: k.wippermann@fz-juelich.de

Keywords: DMFC; synchrotron radiography; through-plane viewing direction; in-plane viewing direction; water droplets; cathode channels

Abstract

Water evolution, distribution and removal in the cathodes of a running direct methanol fuel cell were investigated by means of synchrotron X-ray radiography. Radiographs with a spatial resolution of around 5 µm were taken every 5 s. Special cell designs allowing for through-plane and in-plane viewing were developed, featuring two mirror-symmetrical flow field structures consisting of one channel. Evolution and discharge of water droplets and the occurrence of water accumulations in selected regions of the channels were investigated. These measurements revealed a nonuniform distribution of water in the channels. Both irregular and periodic formation of water droplets were observed. In-plane measurements revealed, that the droplets evolve between adjacent carbon fiber bundles of the GDL. The water distribution within the channel cross section fits very well to the pressure difference between cathode channel inlet and outlet. The quick discharge of water droplets causes sudden decreases of the pressure difference up to 4.5 mbar.

1. Introduction

A critical issue of direct methanol fuel cells (DMFC) is the removal of liquid water from the cathode channels. Compared to hydrogen-powered polymer electrolyte fuel cells (PEFC) the problem is more severe because not only the product water accumulates but, in addition, water and methanol permeate through the membrane. The water partially evaporates and is removed by the flowing air. The remaining liquid water may partially block cathode flow field channels and locally hinder oxygen transport to the catalyst layer and even lead to a significant performance loss as well as enhanced degradation [1-3]. Before work to improve fuel cells can commence, the transport mechanisms of liquid water droplets must be identified and a link established between accumulations of water in the cathode channels and the performance characteristics of direct methanol fuel cells.

Promising techniques for spatially resolved in situ measurements of the water distribution in cell components and flow channels of PEFCS include radiography with neutrons [4-20] or X-rays, the latter generated either by a tube or a synchrotron [21-31]. Neutron radiography is a method that can be used to detect liquid water during cell operation [32, 33]. The formation of water droplets can be visualized with spatial resolutions in the range of 20-100 μm and temporal resolutions from several seconds to minutes [12, 14, 34-36]. If this method is combined with spatially resolved current density measurements, water distributions can be correlated with current density distributions [20, 37].

A method that complements neutron radiography is synchrotron X-ray radiography [21, 38, 39]. Compared to neutron radiography it is – at least at most beamlines – limited to small areas of a few square centimeters. However, this area can be studied with high temporal resolutions and spatial resolutions in the μm range. Synchrotron X-ray radiography, like neutron radiography, offers the possibility to perform measurements in both through-plane or in-plane viewing directions [33]. Various flow distribution geometries permitted water in the cathode channels to be distinguished from water in the anode channels and in the diffusion layers. Principally, two different water transport mechanisms can be identified: On the one hand, a mechanism that continuously filles pores in the diffusion layer until a certain level has been reached. On the other hand, an eruptive mechanism involving the following steps: (i) accumulation of water in pores of the diffusion layer, (ii) merging of water from different

locations to a larger droplet in the cathode channel, (iii) discharge of larger water droplets by convective gas flow [21, 40-43]. The nearly constant frequency of the eruptive mechanism, which mostly involves the same pores, is elevated when the hydrogen flow is reduced [21]. The eruptive transport mechanism was verified by viewing a cell in-plane [44]. Under the selected conditions, at 100 mA/cm², hardly any liquid water was found. However, starting from 600 mA/cm², water accumulated in both the cathode and the anode diffusion layer, particularly near the microporous layer and on the exterior. When the load is increased from 500 mA/cm² to 600 mA/cm², it takes approximately 10 to 15 minutes for an equilibrium state to be reached in both diffusion layers. As a result of the slow diffusion of water on the cathode side through the membrane to the anode, the equilibrium state on the exterior of the anode diffusion layer is achieved last. If the cathodic flow is reduced, a change in the water transport mechanism can be observed [43]. In contrast to the eruptive mechanism, the drops in the cathode channel grow slowly in a periodic fashion and are suddenly removed.

In direct methanol fuel cells with reduced anodic flow and exposure times between 1 s and 4 s, the growth of carbon dioxide bubbles in the anode channels was observed [25]. Through-plane viewing with resolutions between 2 µm and 5 µm make cracks in the catalyst layers visible. They result from the manufacturing process and do not close even after several hours of operation. A speculated swelling of the catalyst layers due to the polymer content was not confirmed. A cell design that can be used for in-plane imaging is based on graphite flow fields with quadratic areas with one horizontally meandering channel being incorporated into each flow field [45, 46]. At two bends, a vertical channel piece is inserted that can be penetrated by X-rays from the side through recesses in the graphite. The wall thickness of the remaining graphite in the beam path is 6.4 mm.

The goal of this study is to use synchrotron X-ray radiography to study the water transport within the DMFC cathode channels and identify starting points for improving the operating stability of direct methanol fuel cells.

2. Experimental

2.1. Cell designs: ‘SYNFRONT’ and ‘SYNCROSS’

With its high spatial resolution, synchrotron radiography is very sensitive to the slightest movement of the fuel cell in the beam, implying strict requirements concerning positional stability. For neutron radiography, it was sufficient to attach the cell to a base plate by using simple aluminum angle brackets that are screwed to the protruding threaded coupling of the tightening screws. For synchrotron radiography, the cells are secured by steel mounts that have a lower compliance and thermal expansion.

The cell design for synchrotron radiography studies in the frontal viewing direction – called ‘SYNFRONT’ – is depicted in Figure 1. The cathodic flow field exhibits straight parallel channels with an in-plane area of 1.5 mm × 1.5 mm and a depth of 0.4 mm (see Figure 1a), while for the anodic flow field simple meandering channels are used (see Figure 1b). The end plates are equipped with three 8 mm × 8 mm large quadratic recesses at the top, in the center, and below (see Figure 1c). They serve as windows for the synchrotron radiation, whereby only one window can be irradiated at a time. The windows above and below are both located above one of the bends of the anodic channel. The green sheet is a printed circuit board (PCB), which served as a current collector.

The cell design for synchrotron radiography in the in-plane viewing direction, denoted as ‘SYNCROSS’, is depicted in Figure 2. The two mirror-symmetric flow field structures consist of one channel with an in-plane area of 1.5 mm × 1.5 mm. The cathodic flow field is shown as an example in Figure 2a. Recesses on the left and right sides are provided for two vertical channel sections. The recesses are 7.5 mm high, 2.5 mm deep, and have a 7-mm wide horizontal gap that contains the width of the channel and the width needed to hold the electrode and the seal. The E-shaped electrode is 3.5 mm wide at this position and the seal is designed to be 1.5 mm wide in each case. To both the right and left of the electrode, a gap of 0.25 mm remains. The electrodes with an area of 12.17 cm² and the seals are all punched out with a punching die.

The MEA including seals and the flow field design is depicted in Figure 2b. When the cell is mounted the recesses form windows for the synchrotron radiation (see Figure 2c). The mounting brackets and

the protruding parts of the printed circuit board (current collector) are arranged such that the vertical channel piece to be studied can be brought close to the scintillator (see Figure 2d).

2.2 MEA Preparation

As a substrate for the anodes and cathodes, AvCarb 1071 HCB carbon fabric supplied by Ballard Material Products was used. It was impregnated with PTFE dispersion TF 5032 supplied by Dyneon and subsequently dried and sintered at 350°C. In a first coating step, a microporous layer of carbon particles (VULCAN XC72 from Cabot) and PTFE (TF 5032 from Dyneon) was applied to the fabric. In a second coating step, the catalyst layer was applied consisting of catalyst material from Johnson Matthey, PTFE (dispersion TF 5032 from Dyneon) and Nafion (dispersion LQ1115 from Ion Power). As catalyst material for the cathode, Johnson Matthey HiSPEC 13100 (71 wt.% Pt/C) was used, while Johnson Matthey HiSPEC 12100 (75 wt.% PtRu/C) was applied as the anode catalyst. The Pt catalyst loadings on the cathode were 1.9 mg/cm² , the PtRu loading on the anode 2.6 mg/cm^2. After the catalyst layer had been dried, it was manually sprayed with Nafion dispersion LQ1115 manufactured by Ion Power. Finally, the anodes and cathodes were shaped as desired and were pressed into finished MEAs for three minutes at a temperature of 130°C and a pressure of 500 N/cm² with an N115 Nafion membrane manufactured by DuPont.

3.3 Synchrotron Radiography

An optical microscope setup was used for the transmission measurements with high spatial and time resolution at the electron storage ring BESSY II of the Helmholtz-Zentrum Berlin, Germany [47] (see schematic drawing, Figure 3a). The synchrotron beam energy was adjusted to 13 keV for the 'SYNFRONT' cell and to 15 keV for the 'SYNCROSS' cell design. The latter energy was higher to provide sufficient transmission through the flow field ribs, as shown in Figure 3b (left part). The time separation between two radiographs for both viewing directions was around 5 s. The detection system contained a 20-µm thick $CdWO_4$ scintillator, a microscope optic combined with a pco4000 camera (4008 × 2672 pixels²). A spatial resolution of about 4 to 5 µm was achieved. For normalization, radio-

graphs without a fuel cell were taken. Specially developed software was used to correct beam artifacts in the radiographs.

3.4 Electrochemical Measurements

Electrical cell performance was recorded with an automated setup for galvanostatic, potentiostatic and impedance measurements called “EIScell”. It was specially developed by ISEA (RWTH Aachen University) for electrochemical measurements [48]. A differential pressure sensor based on the MPX5010DP analog pressure sensor [49] was used to measure the difference in pressure between the cathode inlet and outlet t. In the pressure range between 0 mbar and 100 mbar the differential pressure can be measured with a resolution of about 0.1 mbar. The signal-to-noise ratio was found sufficient to distinguish pressure variations as low as 1 mbar from the background, making the device suitable for the detection of very low differential pressure variations.

The measuring cell is mounted on a base plate which is separated from the end plates by a gap. The PCB is connected to the measurement instrument, which in turn is connected to a measurement computer. A controller keeps the temperature of the measuring cell at 70°C using heating cartridges. The anode was supplied with 1.0 m methanol solution via a peristaltic pump. To supply the cathode, compressed air adjusted with mass flow regulators was used.

3. Results and Discussion

Synchrotron radiography measurements were conducted with both cell designs in either the through-plane or in-plane viewing direction using EIScell. In both cases, the lower recess of each cell was exposed to the radiation, see Figure 1. The measurement cells were loaded with an average current density of 150 mA/cm². The λ values for air and methanol were 4. The time curves of the power density and the cathodic pressure difference of both cells differ for the various flow field geometries, see Figure 4a and b.

In the cell viewed through-plane, a fluctuating power density indicates instable operation. The fluctuations in pressure difference point at varying amounts of water in the cathode channels that reduce the channel cross-section and restrict oxygen supply. In the cell design cell viewed in-plane, pronounced increases in pressure difference occur, followed by sharp drops. Even if the changes in the channel cross-section appear more severe here, an impact on power density is not detectable. Most probably, this is due to the single channel design: unlike multi-channel flow field designs, there is a forced flow through of air, which prevents a complete blocking of the channel and causes a forced air supply of the cathode. Since the cathode channels of both cells are not dried prior to the onset of measurement, the otherwise typical initial increase in pressure difference does not occur.

Figure 5 shows a raw synchrotron radiograph of the measurement cell – 'SYNFRONT' design – in the dry state. The crack structure of anode and cathode catalyst layers, giving rise to small "lands", is clearly visible. The bend in the 1.5-mm deep anode channel appears bright. In contrast, the 0.4-mm deep cathode channels are less prominent. In the lower area, in the projection, the lower milled outlet of the cathode flow field is superimposed on the anode channel. The dark edges of the image on the left and right represent the boundaries of the 8 mm wide window surface in the end plates. Due to the round form of the scintillator, the two corners at the lower left and lower right are not depicted in their entirety. In order to examine the water distribution in the cathode channels, three sections of the image are viewed that each depict a part of a cathode channel that is not superimposed by the anode channel. The three sections of the image are located at the upper edge of the image and are marked with colored frames.

If after beam correction each radiograph is divided by a reference image showing an empty channel section, the average brightness of the resulting images provides information on the water volume in the channel sections under investigation. Brightness values < 1 mean more water compared to the reference image, values > 1 less. The time evolution of normalized brightness is shown in Figure 6a)-c). Since the sections of the image are different in size and because the fraction of visible channel surface in the overall surface of the right section c) is lower in comparison to sections a) and b), the brightness values can be interpreted only qualitatively. Despite this, different conditions in different parts of the

channel sections are evident. In the following, the time-dependent water distribution of the three channel sections is discussed in detail.

Initially, there is hardly any water in the left section (Figure 7). The fluctuations within the first 715 s are mainly due to beam artefacts. Only later does the water volume rise significantly for about 250 s. Figure 7 shows the water distribution in the section at several selected times. During the time period between 565 s and 600 s after the onset of measurement, small droplets form on the right wall of the channel (see white arrow in Figure 7). These droplets are discharged after 605 s. Later, the droplets form again. After 720 s, a droplet evolves in the center of the channel. After 795 s, growth temporarily stops and the size of the droplet decreases slightly. After 800 s, the droplet begins growing again. In the period between 850 s and 915 s after the onset of measurement, the droplet size significantly decreases, after which it increases again. The rapid reductions in droplet size after both 995 s and 1020 s point at a discharge of the droplets in each case. After 1050 s, an accumulation of water moves into the area of the right channel wall. The water remains there briefly before it is discharged. In the further course of experiment, only small droplets form on the right and left channel walls. The irregular evolution of the droplets in the channel center and the occurrence of water accumulations at the right channel wall are reflected by the time curve of the average brightness value.

In the center section, corresponding to Figure 6b, accumulations can be frequently observed which move from the top into the area of the image (see Figure 8). 80 s after the onset of measurement, for example, water is observed on the left and right channel wall. After 85 s, a large part of the channel section is filled with water. This time appears as a minimum in the average brightness value of that area, see Figure 6b. After 90 s, these accumulations of water have been discharged, except for a remnant remaining on the right channel wall. The water volume on the right channel wall first re-increases after 120 s, after which it decreases again after 130 s, whereby a droplet remains at the top of the right channel wall. This is discharged between 155 s and 160 s after the onset of measurement. The water volume increases again after 345 s. Again, part of the water remains on the right channel wall after 360 s. The section of the image 1005 s after the onset of measurement, as well as the sections at some other instants, show three droplets at the top of the left channel wall. Over the course of the measurement, these droplets keep growing at the same location until they are discharged (see white arrows).

The water distribution in the right section – corresponding to Figure 6c – is dominated by the evolution of a droplet at the right edge of the recess, see Figure 9. Between 140 s and 205 s after the onset of measurement the droplet doubles its diameter and is then removed. After this, it grows until the region is filled again. In contrast to the previous case, the accumulation of water remains nearly unchanged for around 60 s. The water is not discharged until 295 s after the onset of measurement and further droplets start to evolve. Between 580 s and 1035 s after the onset of measurement, water entering the channel section from above is only rarely observed and the evolution of droplets temporarily comes to an end. The strongly fluctuating average brightness value in Figure 6c reflects the fluctuating water volumes.

In Figure 10, the in-plane water distribution measured in the 'SYNCROSS' cell at 24 different times is depicted. All images show the difference in water layer thickness Δd_{W} with reference to an image with a flooded anode channel and a dry cathode channel. In the observed channel section, the anode channel is filled with methanol solution and there is no water in the cathode channel prior to the onset of measurement. At the onset of measurement, the first carbon dioxide appears, shown in red in some areas directly to the right of the edge of the the anodic flow field land as negative difference in water layer thickness. 5 s later, a share of carbon dioxide is already found in the entire anode channel. 15 s after the onset of measurement, initially three droplets appear. Later, a fourth droplet appears on the lower edge of the image. Between 55 s and 65 s, a fifth droplet finally forms that grows faster than the other droplets. All droplets evolve between two adjacent carbon fiber bundles of the substrate and remain largely stationary until two of the smaller droplets coalesce after 145 s. After 200 s, the fifth droplet reaches the back wall of the cathode channel. Later, it combines with the already coalesced droplets. After 260 s, the water has been largely removed. The fact that the back wall was also wetted above the fifth droplet allows us to surmise that water from an area of the cell further up is involved in the discharge. Droplets and accumulations of water keep evolving and in some cases are discharged before they reach the back wall. Between 520 s and 525 s after the onset of measurement, an accumulation of water hits the back wall. Although this wall appears to be wetted, the water does not immediately flow off. The reasons for this cannot be determined solely on the basis of the two-dimensional projection. A possible explanation may be that only one edge of the back wall of the channel is wetted

and the accumulation of water does not have any contact to this edge. The changes in colour between the two flow field channels cannot be explained by the formation of carbon dioxide and water only, but are also connected to shifts in the internal layers compared to the reference image. For example, if the catalyst layers move slightly outwards, spurious negative differences in the thickness of the water layer occur along the outer membrane edges, positive differences occurring along the outer edges of the catalyst layers.

Even if one studies only the water distribution of a partial channel section it is possible to correlate the water distribution with the cathodic pressure difference. In Figure 11, the evolution of the pressure difference and the average difference in water layer thickness Δd_W within the cathode channel section is depicted. As the reference image contains a dry cathode channel, this latter difference is identical to the average absolute water layer thickness d_W in the cathode channel section. Times marked by vertical lines in the graph in Figure 11 correspond with the pictures in Figure 10. With the discharge of the accumulations of water 260 s, 405 s and 535 s after the onset of measurement, the pressure difference drops simultaneously. It can be assumed that the water discharge in the cathode channel section studied is accompanied by the discharge of more water in the part of the forced-flow single channel located below it. The temporary drops in pressure difference, for example prior to the first observed discharge of water, can be attributed to the discharge of droplets in the cell area below the irradiated recess.

4. Conclusions and Outlook

Droplet formation in direct methanol fuel cell cathodes was studied by synchrotron X-ray radiography with temporal and spatial resolutions of 5 s and 5 µm, respectively. Measurements in different viewing directions (‘through-plane’ and ‘in-plane’) provide locally and temporally resolved information about the evolution and discharge of water droplets on the cathode GDL and in the cathode channels. The experiments lead to a better understanding of the transport mechanism of liquid water in DMFCs and allow for a targeted improvement of GDL and flow field channel properties with respect to perfor-

mance and degradation. Synchrotron radiography proves to be even more valuable in combination with other *in operando* methods such as pressure difference measurements.

The main results can be summarised as follows:

- nonuniform distribution of water in the cathode channels
- both irregular and periodic formation of water droplets
- the water droplets evolve between adjacent carbon fiber bundles of the GDL
- local evolution/discharge of water
- the water distribution within the channel cross section fits very well to the pressure difference between cathode channel inlet and outlet

In the future, a combination of synchrotron radiography with locally resolved current or impedance measurements could be carried out in analogy to similar studies using neutron radiography [37, 50]. Although it is hardly possible to achieve the high spatial synchrotron resolution of some µm also with spatially resolved local current measurements, it would be interesting to compare synchrotron radiographs with local currents and/or impedances. For example, the differentiation of channel and land effects, as reported by Schneider et al. [51, 52], would be interesting. Schneider et al. used a segmented micro-structured flow field design with a submillimeter resolution for spatially resolved current and impedance measurements [51, 52]. Further synchrotron radiography measurements should also include a variation of the surface properties of the flow fields. In one of our recent publications we reported hydrophilic cathode flow fields to be advantageous with regard to higher power densities, suppression of local current fluctuations and substantial reduction of pressure drop along the cathode channels [50].

Acknowledgements

Funding of the project RuN-PEM (grant number: 03SF0324) by the Federal Ministry of Education and Research (BMBF) is gratefully acknowledged. The authors also like to acknowledge Heinrich Riesemeier from German Federal Institute of Material Research (BAM) for beamline support.

References:

[1] A. A. Kulikovsky, H. Scharmann, K. Wippermann, *Electrochemistry Communications* **2004**, *6*, 729.

[2] A. A. Kulikovsky, *Electrochemistry Communications* **2006**, *8*, 1225.

[3] A. A. Kulikovsky in: *Analytical Modelling of Fuel Cells*, Elsevier, Amsterdam, **2010**, pp. 117.

[4] T. A. Trabold, J. P. Owejan, J. J. Gagliardo, D. L. Jacobson, D. S. Hussey, M. Arif in: *Handbook of fuel cells: Fundamentals, Technology and Applications*, (Eds. W. Vielstich, H. Yokokawa, H.A. Gasteiger), WILEY, New York, **2009**, pp. 658.

[5] D. Kramer, E. Lehmann, G. Frei, P. Vontobel, A. Wokaun, G. G. Scherer, *Nuclear Instruments and Methods in Physics Research Section A: Accelerators, Spectrometers, Detectors and Associated Equipment* **2005**, *542*, 52.

[6] R. J. Bellows, M. Y. Lin, M. Arif, A. K. Thompson, D. Jacobson, *Journal of The Electrochemical Society* **1999**, *146*, 1099

[7] R. Satija, D. L. Jacobson, M. Arif, S. A. Werner, *Journal of Power Sources* **2004**, *129*, 238.

[8] M. A. Hickner, N. P. Siegel, K. S. Chen, D. N. McBrayer, D. S. Hussey, D. L. Jacobson, M. Arif, *Journal of The Electrochemical Society* **2006**, *153*, A902.

[9] M. C. Hatzell, A. Turhan, S. Kim, D. S. Hussey, D. L. Jacobson, M. M. Mench, *Journal of The Electrochemical Society* **2011**, *158*, B717.

[10] N. Pekula, K. Heller, P. A. Chuang, A. Turhan, M. M. Mench, J. S. Brenizer, K. Ünlü, *Nuclear Instruments and Methods in Physics Research Section A: Accelerators, Spectrometers, Detectors and Associated Equipment* **2005**, *542*, 134.

[11] K. T. Cho, A. Turhan, J. H. Lee, J. S. Brenizer, A. K. Heller, L. Shi, M. M. Mench, *Nuclear Instruments and Methods in Physics Research Section A: Accelerators, Spectrometers, Detectors and Associated Equipment* **2009**, *605*, 119.

[12] P. Boillat, G. Frei, E. H. Lehmann, G. G. Scherer, A. Wokaun, *Electrochemical and Solid-State Letters* **2010**, *13*, B25.

[13] A. B. Geiger, A. Tsukada, E. Lehmann, P. Vontobel, A. Wokaun, G. G. Scherer, *Fuel Cells* **2002**, *2*, 92.

[14] P. Boillat, D. Kramer, B. C. Seyfang, G. Frei, E. Lehmann, G. G. Scherer, A. Wokaun, Y. Ichikawa, Y. Tasaki, K. Shinohara, *Electrochemistry Communications* **2008**, *10*, 546.

[15] C. Hartnig, I. Manke, N. Kardjilov, A. Hilger, M. Grünerbel, J. Kaczerowski, J. Banhart, W. Lehnert, *Journal of Power Sources* **2008**, *176*, 452.

[16] I. Manke, C. Hartnig, M. Grünerbel, J. Kaczerowski, W. Lehnert, N. Kardjilov, A. Hilger, J. Banhart, W. Treimer, M. Strobl, *Applied Physics Letters* **2007**, *90*, 184101.

[17] I. Manke, C. Hartnig, N. Kardjilov, M. Messerschmidt, A. Hilger, M. Strobl, W. Lehnert, J. Banhart, *Applied Physics Letters* **2008**, *92*, 244101.

[18] A. Schröder, K. Wippermann, W. Lehnert, D. Stolten, T. Sanders, T. Baumhöfer, N. Kardjilov, A. Hilger, J. Banhart, I. Manke, *Journal of Power Sources* **2010**, *195*, 4765.

[19] Ch. Tötzke, I. Manke, T. Arlt, H. Markötter, N. Kardjilov, A. Hilger, P. krüger, C. Hartnig, J. Scholta, J. Banhart *Journal of Power Sources* **2011**, *196*, 4631.

[20] K. Wippermann, A. Schröder in *Polymer electrolyte membrane and direct methanol fuel cell technology: In situ characterization techniques for low temperature fuel cells (Volume 2), Series volume 31*, (Eds. C. Hartnig, C. Roth), WOODHEAD PUBLISHING, Cambridge, **2012,** pp 214.

[21] I. Manke, C. Hartnig, M. Grünerbel, W. Lehnert, N. Kardjilov, A. Haibel, A. Hilger, J. Banhart, H. Riesemeier, *Applied Physics Letters* **2007**, *90*, 174105.

[22] T. Sasabe, P. Deevanhxay, S. Tsushima, S. Hirai, *Journal of Power Sources* **2011**, *196*, 8197.

[23] T. Sasabe, P. Deevanhxay, S. Tsushima, S. Hirai, *Electrochemistry Communications* **2011**, *13*, 638.

[24] C. Hartnig, I. Manke, R. Kuhn, N. Kardjilov, J. Banhart, W. Lehnert, *Applied Physics Letters* **2008**, *92*, 134106.

[25] C. Hartnig, I. Manke, J. Schloesser, P. Krüger, R. Kuhn, H. Riesemeier, K. Wippermann, J. Banhart, *Electrochemistry Communications* **2009**, *11*, 1559.

[26] H. Markötter, I. Manke, P. Krüger, T. Arlt, J. Haussmann, M. Klages, H. Riesemeier, C. Hartnig, J. Scholta, J. Banhart, *Electrochemistry Communications* **2011**, *13*, 1001.

[27] T. Sasabe, S. Tsushima, S. Hirai, *International Journal of Hydrogen Energy* **2010**, *35*, 11119.

[28] S. J. Lee, S. G. Kim, G. G. Park, C. S. Kim, *International Journal of Hydrogen Energy* **2010**, *35*, 10457.

[29] P. Krüger, H. Markötter, J. Haußmann, M. Klages, T. Arlt, J. Banhart, C. Hartnig, I. Manke, J. Scholta, *Journal of Power Sources* **2011**, *196*, 5250.

[30] P. K. Sinha, P. Halleck, C.-Y. Wang, *Electrochemical and Solid-State Letters* **2006**, *9*, A344.

[31] P. K. Sinha, P. P. Mukherjee, C. Y. Wang, *Journal of Materials Chemistry* **2007**, *17*, 3089.

[32] N. Kardjilov, I. Manke, A. Hilger, M. Strobl, J. Banhart, *Materials Today* **2011**, *14*, 248.

[33] I. Manke, H. Markötter, C. Tötzke, N. Kardjilov, R. Grothausmann, M. Dawson, C. Hartnig, S. Haas, D. Thomas, A. Hoell, C. Genzel, J. Banhart, *Adv. Eng. Mater.* **2011**, *13*, 712.

[34] M. A. Hickner, N. P. Siegel, K. S. Chen, D. S. Hussey, D. L. Jacobson, M. Arif, *Journal of The Electrochemical Society* **2008**, *155*, B427.

[35] S. H. Williams, A. Hilger, N. Kardjilov, I. Manke, M. Strobl, P. A. Douissard, T. Martin, H. Riesemeier, J. Banhart, *Journal of Instrumentation* **2012**, *7*, P02014.

[36] N. Kardjilov, M. Dawson, A. Hilger, I. Manke, M. Strobl, D. Penumadu, K. H. Kim, F. Garcia-Moreno, J. Banhart *Nuclear Instruments and Methods in Physics Research Section A: Accelerators, Spectrometers, Detectors and Associated Equipment* **2011**, *651*, 95.

[37] A. Schröder, K. Wippermann, J. Mergel, W. Lehnert, D. Stolten, T. Sanders, T. Baumhöfer, D. U. Sauer, I. Manke, N. Kardjilov, A. Hilger, J. Schloesser, J. Banhart, C. Hartnig, *Electrochemistry Communications* **2009**, *11*, 1606.

[38] J. Banhart, A. Borbely, K. Dzieciol, F. Garcia-Moreno, I. Manke, N. Kardjilov, A. R. Kaysser-Pyzalla, M. Strobl, W. Treimer, *International Journal of Materials Research* **2010**, *101*, 1069.

[39] J. H. Kinney, M. C. Nichols, *Annual Review of Materials Science* **1992**, *22*, 121.

[40] S. Litster, D. Sinton, N. Djilali, *Journal of Power Sources* **2006**, *154*, 95.

[41] X. Zhu, P. C. Sui, N. Djilali, *Journal of Power Sources* **2007**, *172*, 287.

[42] X. Zhu, P. C. Sui, N. Djilali, *Microfluidics and Nanofluidics* **2008**, *4*, 543.

[43] I. Manke, C. Hartnig, N. Kardjilov, H. Riesemeier, J. Goebbels, R. Kuhn, P. Krüger, J. Banhart, *Fuel Cells* **2010**, *10*, 26.

[44] C. Hartnig, I. Manke, R. Kuhn, S. Kleinau, J. Goebbels, J. Banhart, *Journal of Power Sources* **2009**, *188*, 468.

[45] R. Kuhn, J. Scholta, P. Krüger, C. Hartnig, W. Lehnert, T. Arlt, I. Manke, *Journal of Power Sources* **2011**, *196*, 5231.

[46] W. Maier, T. Arlt, C. Wannek, I. Manke, H. Riesemeier, P. Krüger, J. Scholta, W. Lehnert, J. Banhart, D. Stolten, *Electrochemistry Communications* **2010**, *12*, 1436.

[47] W. Görner, M. P. Hentschel, B. R. Müller, H. Riesemeier, M. Krumrey, G. Ulm, W. Diete, U. Klein, R. Frahm, *Nuclear Instruments and Methods in Physics Research Section A: Accelerators, Spectrometers, Detectors and Associated Equipment* **2001**, *467-468*, 703.

[48] H. Blanke, M. Kiel, T. Sanders, T. Baumhöfer, B. Fricke, D.-U. Sauer, *Haus der Technik - Technische Mitteilungen* **2006**, *99*, 184.

[49] Integrated Silicon Pressure Sensor, in, Freescale Semiconductor.

[50] A. Schröder, K. Wippermann, G. Zehl, D. Stolten, *Electrochemistry Communications* **2010**, *12*, 1318.

[51] I. A. Schneider, S. von Dahlen, A. Wokaun, G. G. Scherer, *Journal of The Electrochemical Society* **2010**, *157*, B338.

[52] I. A. Schneider, M. H. Bayer, S. von Dahlen, *Journal of The Electrochemical Society* **2011**, *158*, B343.

Figure Captions:

Figure 1: Imaging in the through-plane viewing direction. Flow fields of a) cathode, b) anode. c) Cell design ‘SYNFRONT’ with mounting brackets, view onto cathode side. Rectangles in a) and b) show the field of view of the camera system, see Figure 5.

Figure 2: Measurements in the in-plane viewing direction. a) Cathodic flow field, b) MEA with seals, c) cell design 'SYNCROSS' with mounting brackets with a view towards the windows for synchrotron radiation, d) view onto the cathode side. The arrow in a) specifies the beam direction.

Figure 3: a) Schematic drawing of synchrotron X-ray imaging; b) schemes of different viewing directions.

Figure 4: Operating behavior of cells in, a) the through-plane viewing direction and, b) the in-plane viewing direction. The parameters applied were j = 150 mA/cm^2, λ_{MeOH} = 4, λ_{air} = 4, T = 70°C.

Figure 5: Raw synchrotron radiograph of a cell of design type 'SYNFRONT', including meander anode flow field and channel cathode flow field. View of lower recess. Process parameters were j = 150 mA/cm^2, λ_{MeOH} = 4, λ_{air} = 4, T = 70°C. Colours correspond to Figure 6a-c.

Figure 6: Brightness values of the three cathode channel sections a), b) and c) marked in Figure 5. Transmission values are given.

Figure 7: Water distribution in the left cathode channel section, marked in red in Figure 5a. Normalized images, process parameters j = 150 mA/cm^2, λ_{MeOH} = 4, λ_{air} = 4, T = 70°C.

Figure 8: Same as Figure 7 for the section marked in green in Figure 5b.

Figure 9: Same as Figure 7 for the section marked in blue in Figure 5c.

Figure 10: Water distribution in the lower recess of the cell design 'SYNCROSS'.
Δd_W: difference in water layer thickness with respect to the reference radiograph. Normalized and colored. Process parameters were j = 150 mA/cm^2, λ_{MeOH} = 4, λ_{air} = 4, T = 70°C.

Figure 11: Correlation between pressure difference and water layer thickness in the cell design 'SYNCROSS'. d_W: average water layer thickness in the cathode section. Process parameters are j = 150 mA/cm^2, λ_{MeOH} = 4, λ_{air} = 4, T = 70°C.

Figures:

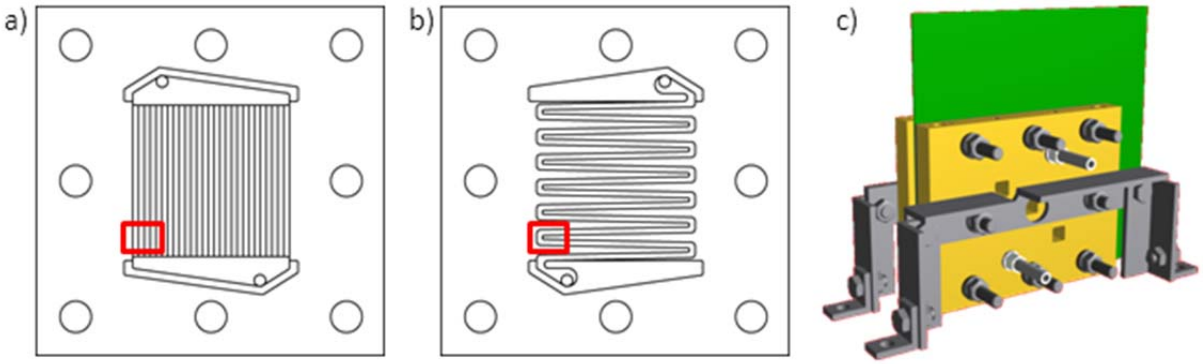

Fig.1

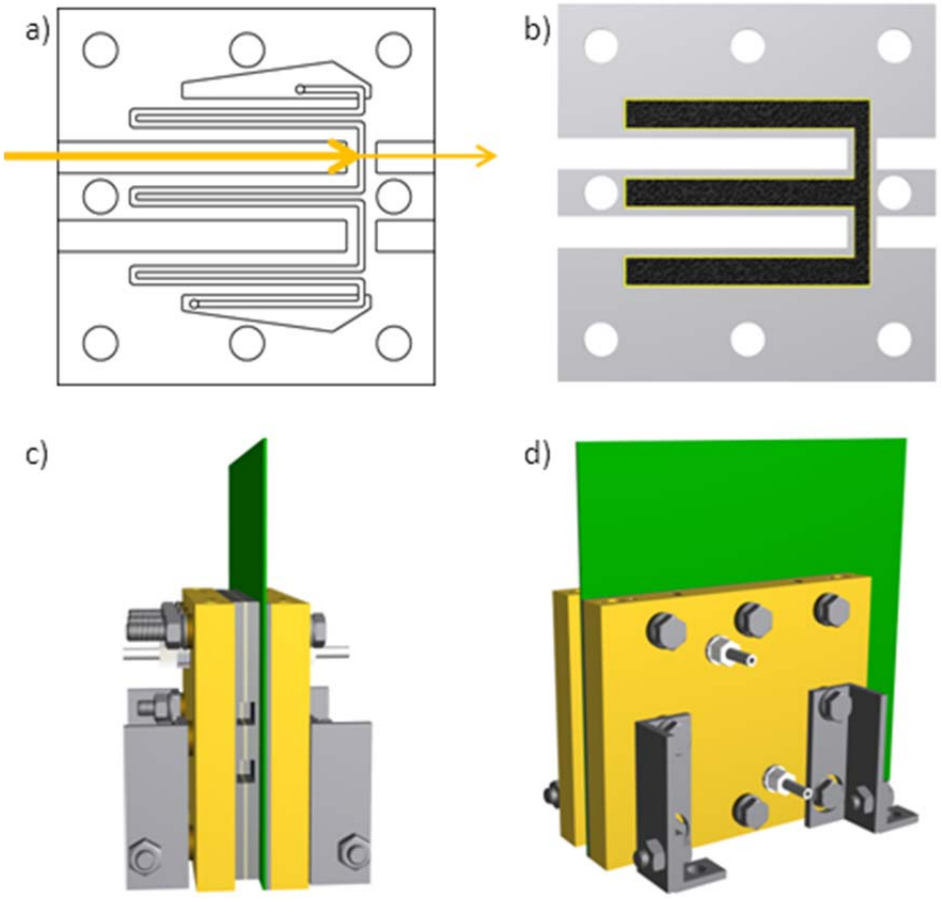

Fig.2

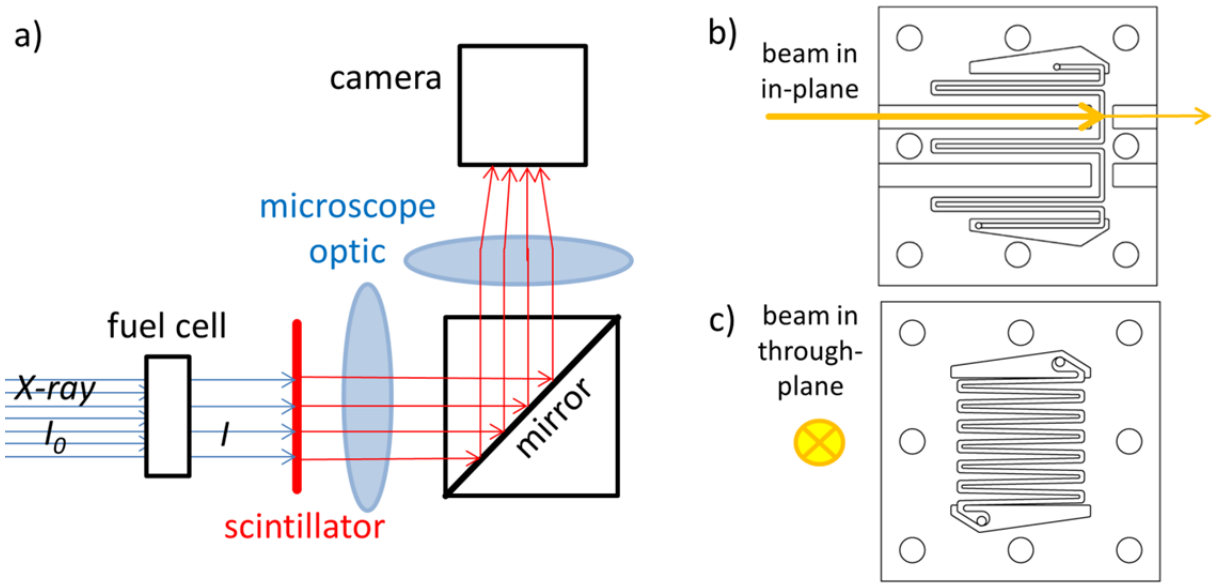
a)
camera
microscope
optic
fuel cell
X-ray
I_0
I
mirror
scintillator
b)
beam in
in-plane
c)
beam in
through-
plane

Fig.3

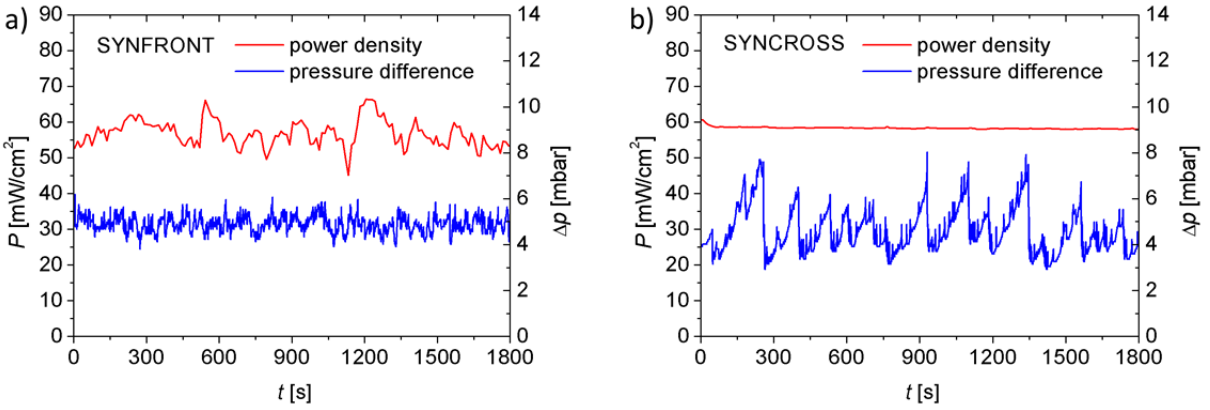
a)
SYNFRONT
power density
pressure difference
P [mW/cm²]
Δp [mbar]
t [s]
b)
SYNCROSS
power density
pressure difference
P [mW/cm²]
Δp [mbar]
t [s]

Fig.4

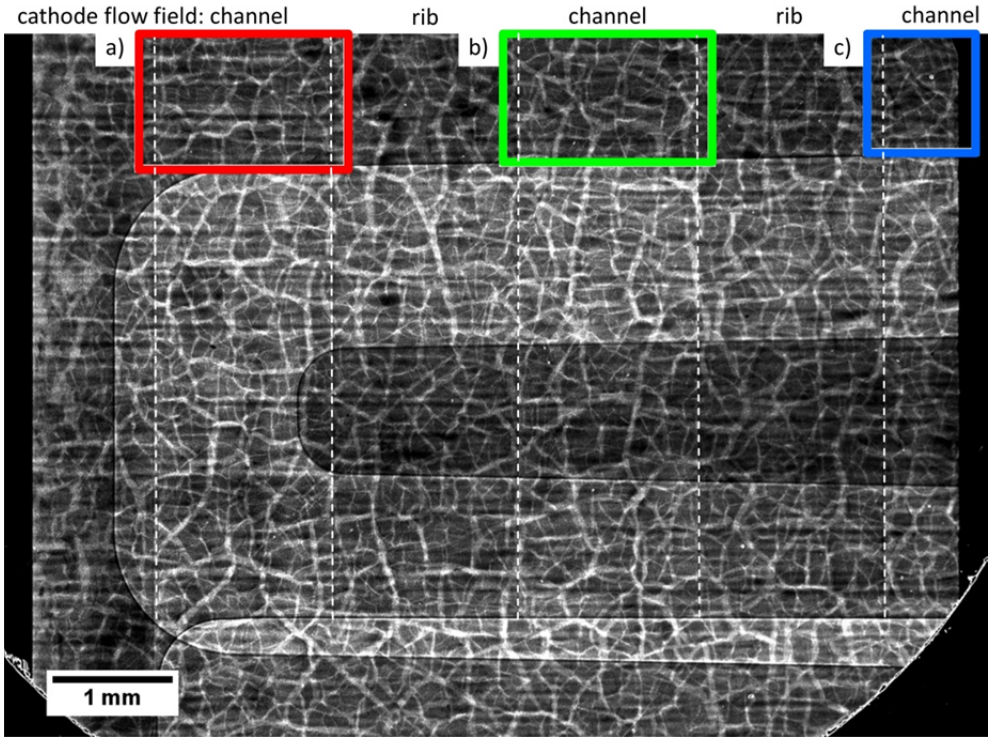
cathode flow field: channel
rib
channel
rib
channel
a)
b)
c)
1 mm

Fig.5

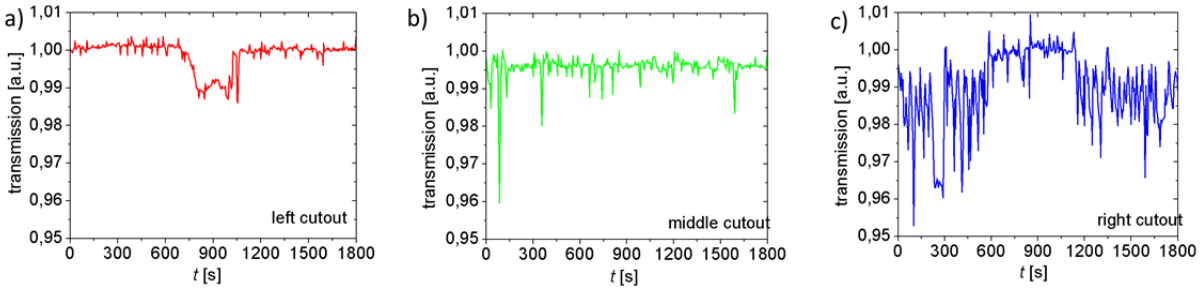
a)
b)
c)
transmission [a.u.]
1,01
1,00
0,99
0,98
0,97
0,96
0,95
0
300
600
900
1200
1500
1800
t [s]
left cutout
middle cutout
right cutout

Fig.6

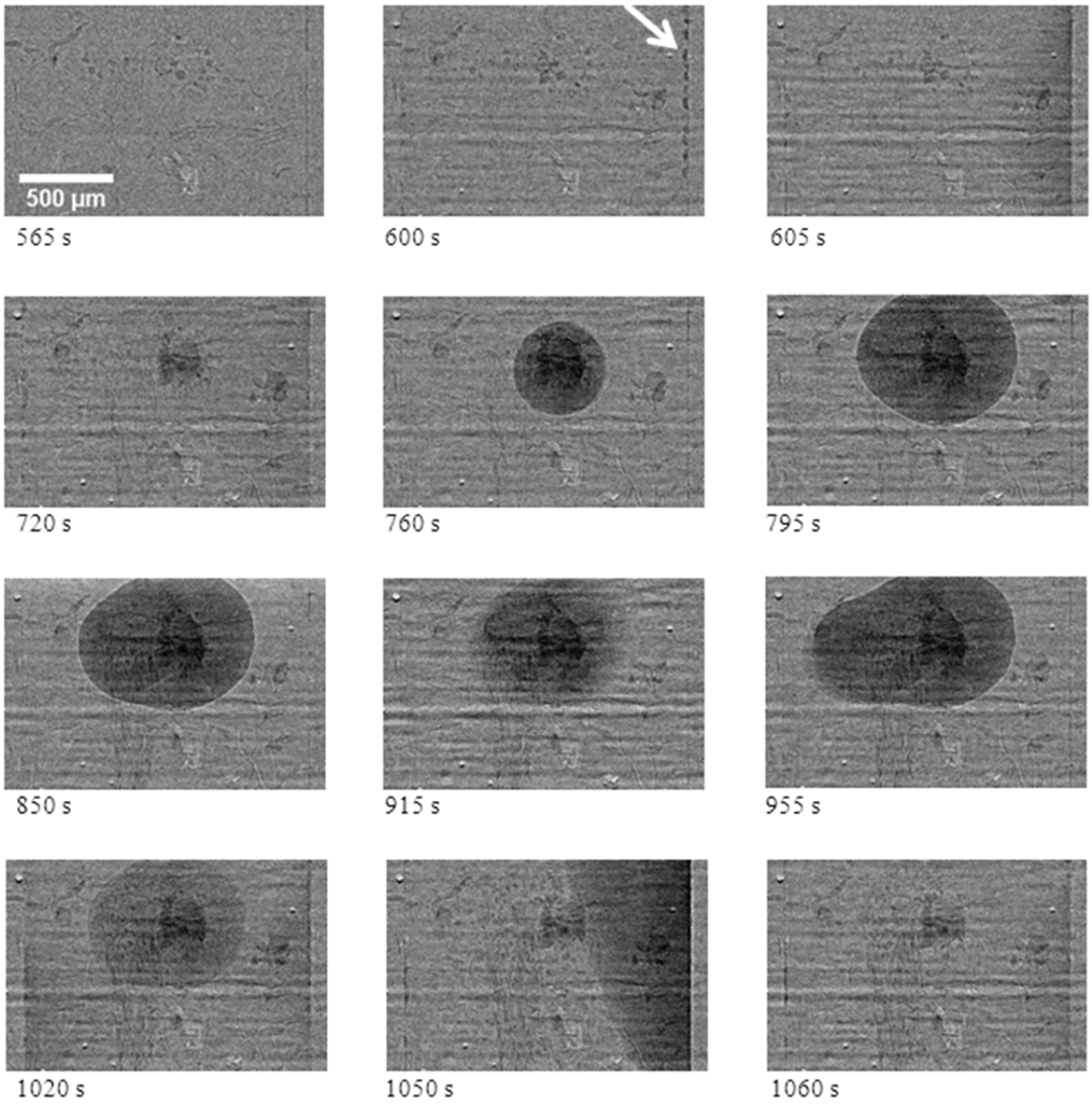
500 µm
565 s
600 s
605 s
720 s
760 s
795 s
850 s
915 s
955 s
1020 s
1050 s
1060 s

Fig.7

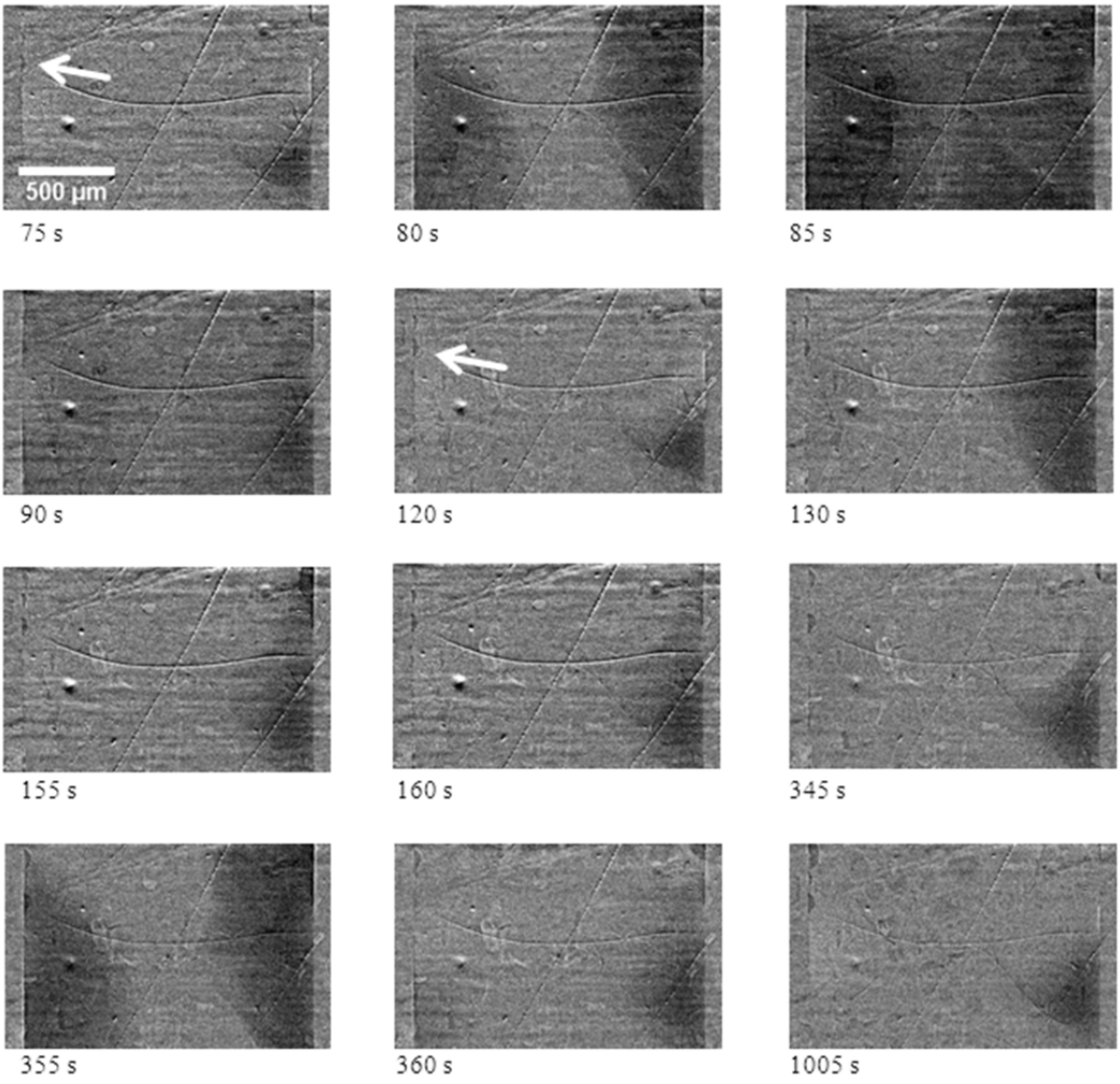
500 µm
75 s
80 s
85 s
90 s
120 s
130 s
155 s
160 s
345 s
355 s
360 s
1005 s

Fig.8

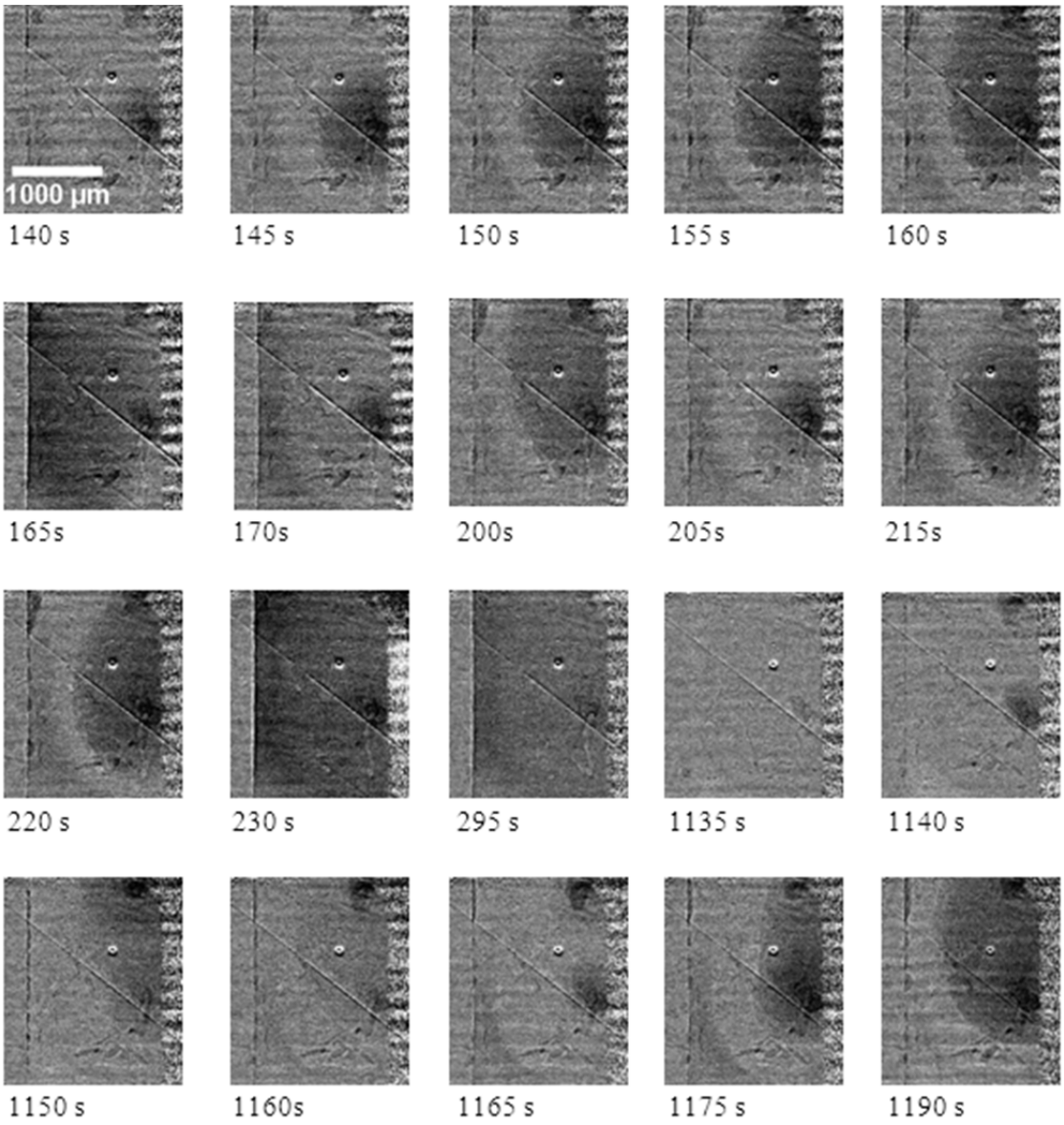
1000 µm
140 s
145 s
150 s
155 s
160 s
165s
170s
200s
205s
215s
220 s
230 s
295 s
1135 s
1140 s
1150 s
1160s
1165 s
1175 s
1190 s

Fig.9

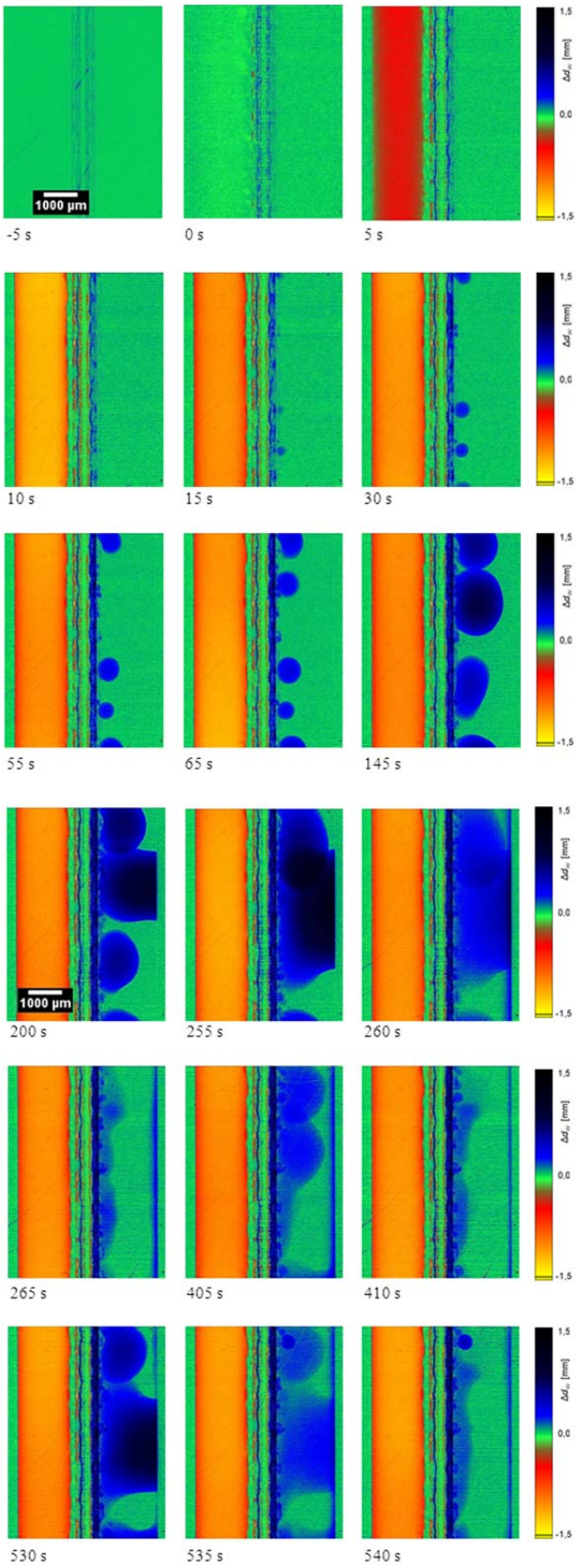
1000 µm
-5 s
0 s
5 s
10 s
15 s
30 s
55 s
65 s
145 s
1000 µm
200 s
255 s
260 s
265 s
405 s
410 s
530 s
535 s
540 s
1,5
0,0
-1,5

Fig.10

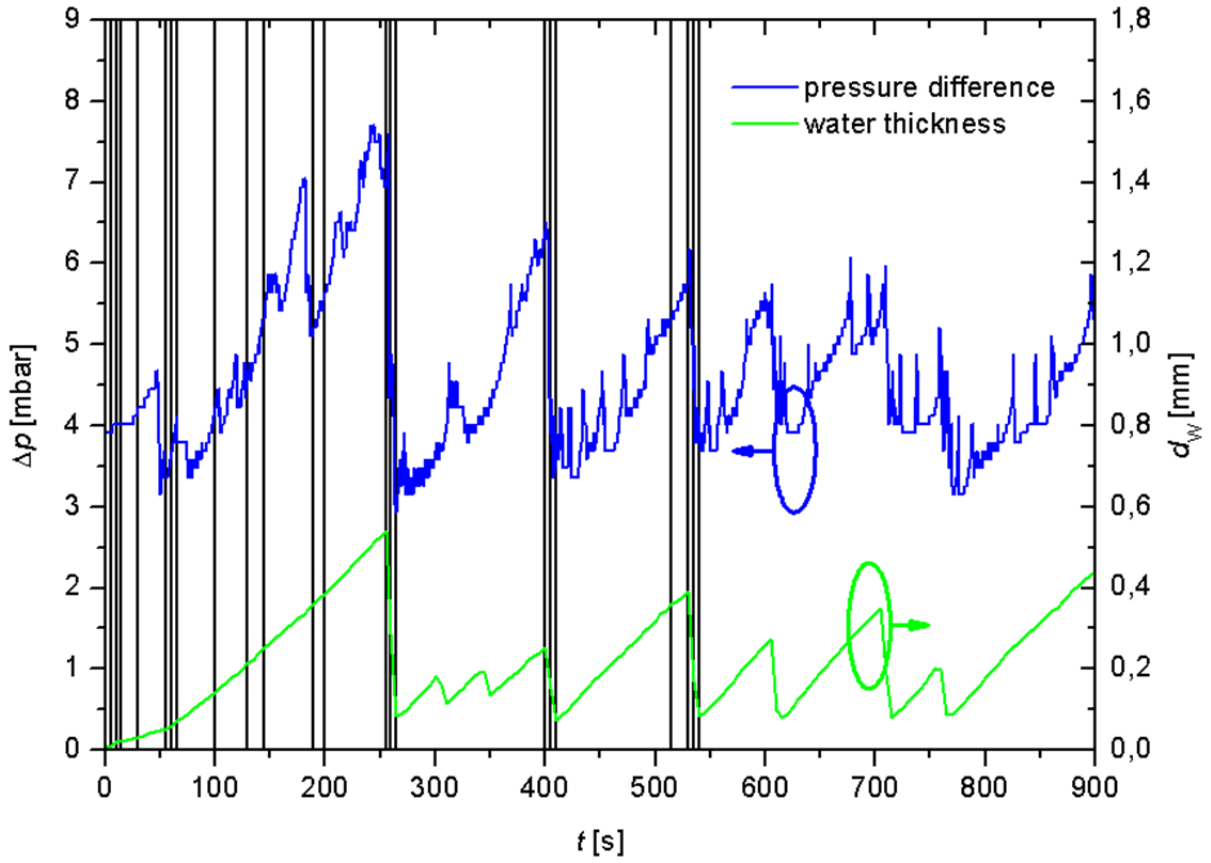
pressure difference
water thickness
Δp [mbar]
d_W [mm]
t [s]
0
1
2
3
4
5
6
7
8
9
0,0
0,2
0,4
0,6
0,8
1,0
1,2
1,4
1,6
1,8
0
100
200
300
400
500
600
700
800
900

Fig.11